Published in final edited form as:

Acta Biomater. 2020 July 15; 111: 129–140. doi:10.1016/j.actbio.2020.04.047.

3D-printed scaffolds with carbon nanotubes for bone tissue engineering: Fast and homogeneous one-step functionalization

Xifeng Liu[a,b], **Matthew N. George**[a,b], **Sungjo Park**[c], **A. Lee Miller II**[b], **Bipin Gaihre**[a,b], **Linli Li**[a,b], **Brian E. Waletzki**[b], **Andre Terzic**[c], **Michael J. Yaszemski**[a,b], **Lichun Lu**[a,b,*]

[a]Department of Physiology and Biomedical Engineering, Mayo Clinic, Rochester, MN 55905, USA

[b]Department of Orthopedic Surgery, Mayo Clinic, Rochester, MN 55905, USA

[c]Department of Cardiovascular Diseases and Center for Regenerative Medicine, Mayo Clinic, Rochester, MN 55905, USA

Abstract

Three-dimensional (3D) printing is a promising technology for tissue engineering. However, 3D-printing methods are limited in their ability to produce desired microscale features or electrochemical properties in support of robust cell adhesion, proliferation, and differentiation. This study addresses this deficiency by proposing an integrated, one-step, method to increase the cytocompatibility of 3D-printed scaffolds through functionalization leveraging conductive carbon nanotubes (CNTs). To this end, CNTs were first sonicated with water-soluble single-stranded deoxyribonucleic acid (ssDNA) to generate a negatively charged ssDNA@CNT nano-complex. Concomitantly, 3D-printed poly(propylene fumarate) (PPF) scaffolds were ammonolyzed to introduce free amine groups, which can take on a positive surface charge in water. The ssDNA@CNT nano-complex was then applied to 3D-printed scaffolds through a simple one-step coating utilizing electric-static force. This fast and facile functionalization step resulted in a homogenous and non-toxic coating of CNTs to the surface, which significantly improved the adhesion, proliferation, and differentiation of pre-osteoblast cells. In addition, the CNT based conductive coating layer enabled modulation of cell behavior through electrical stimuli (ES) leading to cellular proliferation and osteogenic gene marker expression, including alkaline phosphatase (ALP), osteocalcin (OCN), and osteopontin (OPN). Collectively, these data provide the foundation for a one-step functionalization method for simple, fast, and effective functionalization of 3D printed scaffolds that support enhanced cell adhesion, proliferation, and differentiation, especially when employed in conjunction with ES.

Keywords

3d-printing; Carbon nanotube; Tissue engineering; Osteogenesis; Electrical stimulation

---

[*]Corresponding author at: Department of Physiology and Biomedical Engineering, Mayo Clinic, Rochester, MN 55905, USA. Lu.Lichun@mayo.edu (L. Lu).

Supplementary materials
Supplementary material associated with this article can be found, in the online version, at doi:10.1016/j.actbio.2020.04.047.

Declaration of Competing Interest
The authors declare no competing financial interest.

1. Introduction

Three-dimensional (3D) printing is a rapidly advancing technology with applications in a variety of fields including engineering, manufacturing, and medicine [1, 2]. For bone tissue engineering, 3D printing holds great promise in the development of implantable scaffolds that are embedded within bone defects or fracture sites, providing structural support and a substrate for cell growth and tissue regeneration. 3D-printing approaches have an advantage over traditional methods due to the wide array of sophisticated architectures that can be printed to replicate the hierarchical organization of composite biomaterials, such as cartilage and bone [3]. Increased cell-scaffold complexity facilitates tissue ingrowth and implant-tissue integration, especially when partnered with 3D-printable inks that are made from biodegradable polymers and produce nontoxic byproducts [3].

Biodegradable polymers that have been used in the development of implantable bone scaffolds include poly(lactic-co-glycolic acid) (PLGA) [4], poly(L-lactic acid) (PLLA) [5], poly(ε-caprolactone) (PCL) [6–8], and poly(propylene fumarate) (PPF) [9]. Among these polymers, PPF, which possesses double bonds within the polymer backbone, has been used to produce crosslinked scaffolds with rigidities that are favorable for bone regeneration applications [10–12]. To this end, *in vitro* assessment of functionalized PPF scaffolds in our laboratory has observed robust osteoblast attachment, proliferation, and tissue mineralization [10, 12, 13]. These results have since been confirmed *in vivo* through the implantation of 3D-printed PPF-based scaffolds produced using stereolithography in rabbits, resulting in extraordinary bone regeneration after 6 weeks [14].

Carbon nanotubes (CNTs) are cylindrical molecules made from bent two-dimensional (2D) graphene sheets. CNTs are known for extraordinary mechanical stiffness and electrical conductivity [15], leading to their inclusion in a variety of tissue engineering applications in an effort to promote *in situ* drug delivery, support the mechanical stabilization of implants, and enhance the surface conductivity of neural tubes [16–20]. As electrically-active cells, nerve cells are sensitive to conductive substrates, with previous studies confirming CNT substrates stimulate neurite extension and nerve cell growth [21–27]. A similar result has been observed with bone, with electrical stimulation enhancing the osteogenesis of mouse pre-osteoblast cells *in vitro* [28]. Comparable increases in osteogenic gene expression have been observed *in vivo* using large defect sites in rat femurs as a model, with the additional observation that electrical stimulation also led to enhanced bone and vessel formation [29].

In previous studies, CNTs showed promising results for bone repair [30, 31]. However, despite the fact that CNTs have been successfully employed previously as an electrically conductive layer for cell stimulation, two issues remain that prevent their wider adoption in tissue engineering applications. The first is molecular aggregation; CNTs quickly form aggregates and precipitate in solution, causing difficulty for further processing using CNT dispersions [32–34]. The second commonly encountered issue is biocompatibility. In their native form CNTs are mildly cytotoxic, limiting cell attachment and growth [35–37]. Recent studies have shown that the dispersion of CNTs can be largely improved through the modification of surfaces with a water-soluble component layer [35–37], a result that can be achieved through the co-mingling of CNTs with single-strand DNA (ssDNA) [38–43].

The molecular entanglement of CNT and ssDNA (ssDNA@ CNT) also has been shown to significantly reduce the cytotoxicity of CNT bundles in both *in vitro* and *in vivo* applications [44–46].

In this study, we propose a simple one-step method to enhance the cytocompatibility of cellular scaffolds through the functionalization of 3D-printed scaffolds with CNTs, using a ssDNA@CNT solution generated through the mixture of CNTs and ssDNA fragments under ultra-sonication (Fig. 1a). Utilizing electrostatic forces, ssDNA@CNTs were functionalized onto 3D-printed PPF scaffolds that were positively charged by ammonolysis (Fig. 1b). After functionalization, the surface properties of 3D printed scaffolds were extensively evaluated. Pre-osteoblast behaviors on functionalized scaffolds were investigated including cell proliferation, spreading, shape, filament development, and osteogenic differentiation. In addition, electrical stimulation was applied to these scaffolds and pre-osteoblast behaviors were further evaluated (Fig. 1c). The expression of osteogenic markers in pre-osteoblast cells on functionalized 3D-printed scaffolds were also evaluated using quantitative real-time PCR analysis.

2. Materials and methods

2.1. Polymer synthesis

3D-printed scaffolds were manufactured using a photo-crosslinkable resin made from poly(propylene fumarate) (PPF), the synthesis for which has been previously referenced in publications from our laboratory [47]. Concisely, diethyl fumarate monomer (DEF, Sigma Aldrich, Milwaukee, WI) was mixed with an excess of 1,2-propylene glycol under flowing nitrogen while stirring. Hydroquinone was added as a cross-linking inhibitor as well as zinc chloride as a catalyst. The reaction was kept at 100 °C for 1 hthen increased to 150 °C for another 7 h. Propylene fumarate was further polymerized to poly(propylene fumarate) by condensation for another 4 h at 130 °C while removing any propylene glycol byproducts under constant pumping vacuum.

2.2. Scaffold printing by 3D stereolithography

2.2.1. Polymeric resin formation—An ultraviolet (UV) curable resin was prepared by dissolving dried PPF in a cross-linkable diethyl fumarate monomer (DEF; PPF/DEF wt:wt ratio = 60:40) while stirring at 37 °C for 1 d under protection from light. After all polymers were fully dissolved, 1.5 wt% of bisacrylphosphrine oxide (BAPO, Ciba Specialty Chemicals, Tarrytown, NY) was added to the mixture, resulting in a PPF/DEF/BAPO resin that was used immediately for 3D printing.

2.2.2. Computer-aided design (CAD) of 3D scaffolds—3D scaffold models comprised of orthogonal cubic-lattice disks with a distribution of pores in each plane were designed using CAD software (SolidWorks Corp., Concord, MA), as described previously [13]. The overall model dimensions were 5 mm square (length, width, and height), with nine 1 mm square pores on each face, separated by ridges with a thickness of 0.5 mm.

2.2.3. Scaffold printing by 3D stereolithography—

3D scaffold models generated in CAD were converted to stereolithography (STL) file format, which was used to further generate 2D slice data (BFF) files using 3D Lightyear software, setting the layer thickness to 101.6-μm per layer in preparation for printing. A Viper si2 stereolithography system (3D Systems, Valencia, CA) equipped with 365 nm UV laser was used to execute the BFF files, crosslinking the PPF/DEF polymer resin layer-by-layer as it was deposited to produce the desired 3D structure.

2.2.4. Post-printing cure and washing—

After stereolithographic printing, scaffolds were gently rinsed with acetone followed by absolute ethanol to remove any uncured resin on the surface. After drying, cleaned scaffolds were post-cured with UV light for an additional 2 h. Cured scaffolds were transferred into a Soxhlet extraction apparatus and extracted for 3 days using a mixture of ethanol and tetrahydrofuran (50/50). This step makes 3D scaffolds biocompatible by extracting out toxic sol fractions.

2.3. Fabrication of ssDNA@CNT nanocomposite

Carbon nanotubes (Sigma Aldrich Co., Milwaukee, WI) were sonicated in deionized and distilled ultra-pure Millipore H_2O (ddH_2O) to obtain a homogeneous dispersion with a concentration of 1 mg/mL. Similarly, single-stranded deoxyribonucleic acid extracted from human placenta (ssDNA; Sigma Aldrich Co., Milwaukee, WI) was diluted to 0.2 mg/mL in ddH_2O. A ssDNA@CNT solution was then prepared by mixing equal volumes of the prepared CNT and ssDNA solutions, resulting in a final CNT concentration of 0.5 mg/mL and ssDNA concentration of 0.1 mg/mL. The mixture was sonicated for 1 hr using an ice bath sonicator (Elmasonic S10, Elma Schmidbauer GmbH, Germany) to fully bind the ssDNA fragments to the CNTs and then centrifuged to remove nondispersed particles, filtering the supernatant using a disk membrane filter (pore size 0.2 μm) in accordance with previous studies [40]. The filtered ssDNA@CNT composite was then washed with an excessive amount of ultra-pure Millipore water to remove unbound DNA and carbon debris. The morphology of the starting CNT solution and ssDNA@CNT nanocomposite solution were imaged using a scanning electron microscope (SEM, S-4700, Hitachi Instruments, Tokyo, Japan) under voltage of 5 kV and a transmission electron microscope (TEM, 1200-EX II, JEOL Inc., Japan) under 80 kV voltage. The morphology of the CNT and ssDNA@CNT nanocomposites were determined using an atomic force microscope (AFM) using the Nanoscope IV PicoForce Multimode AFM machine (Bruker, Santa Barbara, CA) [48].

For zeta potential tests, CNT and ssDNA@CNT were dispersed by sonication for 10 min in ddH_2O at a density of 0.5 mg/mL and subsequently measured using a Zetasizer Nano ZS (Malvern Instruments). The conductivity of CNT and ssDNA@CNT were compared as both a dispersion in solution and also as a solid pellet. For the solution test, CNT and ssDNA@CNT solutions (0.5 mg/mL) were dispersed by sonication in ddH_2O for 10 min. The current of both composite solutions was recorded on a Zetasizer Nano ZS (Malvern Instruments) and was used to calculate conductivity, averaging the results of 10 tests. For solid conductivity tests, dried CNT and ssDNA@CNT nanocomposites were pressed under 3000 psi pressure to form sheet-like pellets with a thickness of approximately 100 μm, following previously published methods [49]. Pellets were then cut into rectangular shapes, measuring the resistance (R) across the pellet using a multimeter (34461A Digital Multimeter, 6½ Digit, Keysight Technologies, Santa Rosa, CA). The electrical resistivity (ρ) of the CNT and ssDNA@CNT nanocomposites was calculated by the following equation:

$$\rho = \mathrm{R}\frac{A}{L} = R\frac{W \times H}{L}, \tag{1}$$

where A represents the sheet cross-sectional area, L represents the sheet length, and W and H represent the width and height of the CNT and ssDNA@CNT sheet, respectively. The electric conductivity (σ) in siemens per meter (S/m) of the CNT and ssDNA@CNT sheets was calculated by equation,

$$\sigma = \frac{1}{\rho}, \tag{2}$$

2.4. Functionalization of 3D scaffolds

3D-printed PPF scaffolds were ammonolyzed following previously established protocols to produce positively charged PPFA scaffolds [50]. Briefly, scaffolds were immersed for 30 min at 60 °C in an isopropyl alcohol (100 mL) solution containing 6.0 g of hexamethylenediamine (Sigma Aldrich, Milwaukee, WI). After the ammonolysis reaction, scaffolds were immersed for 2 d in excess ddH$_2$O with frequent water changes to remove any unreacted hexamethylenediamine, dried under vacuum, and stored for further use.

3D-printed PPFA scaffolds were separated into one of four treatment groups and functionalized with either (1) ddH$_2$O (negative control), (2) ssDNA (0.1 mg/mL), (3) CNT (0.5 mg/mL), or (4) ssDNA@CNT (0.1 mg/mL ssDNA and 0.5 mg/mL CNT). In all cases, treatments were preceded by immersing dried 3D-PPFA scaffolds for 10 min in ddH$_2$O to reactivate the surficial amine groups. Activated 3D-PPFA scaffolds were then submerged in each respective treatment for 1 hr under constant agitation, followed by immersion in excess ddH$_2$O for 10 min to remove any unattached components. Cleaned scaffolds were then dried to obtain (1) 3D-PPFA, (2) 3D-PPFA-ssDNA, (3) 3D-PPFA-CNT, or (4) 3D-PPFA-ssDNA@CNT scaffolds, respectively. The surface morphologies of functionalized scaffolds within each treatment group were investigated using a scanning electron microscope (S-4700, Hitachi Instruments, Tokyo, Japan) under a voltage of 5 kV, sputter-coating the surface of each scaffold with a thin layer of conductive gold-palladium to reduce charging.

2.5. Biocompatibility of functionalized 3D-printed scaffolds

2.5.1. Cytotoxicity of the leaching medium—

To determine the cytotoxicity of any molecular components that emanate from 3D-printed scaffolds, scaffolds from each treatment group were cocultured with MC3T3 pre-osteoblast cells in 6-well tissue culture plates fitted with transwell chambers that separated scaffolds from coming in direct contact with cells (mesh size 3 μm; Corning). Functionalized scaffolds were sterilized under UV irradiation for 4 Hand subsequently placed within transwell chambers positioned directly above cultures seeded with 15,000 cells/well. Wells were then filled with α-MEM medium

(Gibco) supplemented with 10% FBS and 1% Penn/Strep, taking care to immerse scaffolds in media to allow nanocomposites to release into cell cultures. After co-cultured for 2, 4, and 6 days at 37 °C (relative humidity = 95%, CO_2 = 5%), the cell density in each well was determined using the MTS assay (CellTiter 96, Promega, Madison, WI), recording the optical absorbance at 490 nm using a UV–vis absorbance microplate reader (SpectraMax Plus 384, Molecular Devices, Sunnyvale, CA).

2.5.2. Direct culture cytotoxicity—To determine the effect that functionalization treatments had on cell survival, MC3T3 pre-osteoblast cells were cultured directly on 3D-printed scaffolds from each treatment group. Scaffolds were adhered to the bottom of 48-well TCPS plates using sterile silicone-based high vacuum grease (Dow Corning, Midland, MI), seeding cells at a density of 40,000 cells/well in the α-MEM medium. Plates were then incubated for 2 days at 37 °C (relative humidity = 95%, CO_2 = 5%) after which scaffolds were removed and rinsed with PBS three times before being stained using the LIVE/DEAD ® Cell Imaging Kit (Thermo Fisher Scientific). Live (green) and dead (red) cells were then imaged using an Axiovert A1 Zeiss light microscope (Carl Zeiss, Germany).

2.6. Pre-osteoblast proliferation on 3D-printed scaffolds

The proliferation of pre-osteoblasts cultured directly on functionalized 3D-PPFA scaffolds was determined by adhering sterilized scaffolds from each treatment group to the bottom of 48-well TCPS plates and seeding each well with MC3T3 pre-osteoblast cells at a density of 40,000 cells/well. The bottom of each well was covered with sterile silicon grease in an effort to prevent cell attachment to the bottom and sides of each well. Cells were cultured in a non-osteogenic α-MEM medium at 37 °C (relative humidity = 95%, CO_2 = 5%), for 1, 4, and 7 d, measuring the cell count within each well using the MTS assay as previously described.

To observe the distribution pattern of pre-osteoblasts on the 3D-printed scaffolds, scaffolds were removed at discrete time points and cells were fixed using 4% paraformaldehyde (PFA). Fixed cells were repeatedly rinsed with PBS to remove PFA residue followed by permeabilization using 0.2% Triton X-100. Permeabilized cells were placed in 1% bovine serum albumin (BSA) for 1 h at 37 °C with gentle shaking to block the non-specific binding sites in cells. After washing, the blocked pre-osteoblasts were immunostained for 1 h at 37 °C with 1:200 diluted rhodamine-phalloidin (RP, Cytoskeleton Inc., Denver, CO, USA) to label cellular filaments and another 10 min with 4’,6-diamidino-2-phenylindole (DAPI) to label cell nuclei. The immuno-fluorescence labeled cells on 3D-printed scaffolds were instantaneously imaged using an inverted laser scanning confocal microscope (LSM 780, Carl Zeiss, Germany).

For single cellular morphology and focal adhesion imaging, pre-osteoblasts on the 3D-printed scaffolds were fixed, perme-abilized and blocked as described above. Pre-treated cells were then immune-stained with for 1 h at 37 °C with 1:50 diluted anti-vinculin–FITC antibody (Sigma-Aldrich Co., Milwaukee, WI) to label vinculin and another hour at 37 °C with 1:200 diluted rhodamine-phalloidin (RP, Cytoskeleton Inc, Denver, CO, USA) to label cellular filaments. Cell nuclei were further labeled by 10 min staining with 4’,6-

diamidino-2-phenylindole (DAPI). The immunofluorescence labeled cells on the 3D-printed scaffolds were imaged using an inverted laser scanning confocal microscope (Carl Zeiss).

2.7. Electrical stimulation

The effect of electrical stimulation on the proliferation of pre-osteoblast cells growing on each type of functionalized 3D-printed scaffolds was evaluated using a C-Pace EP cell culture stimulator with assortative 12-well plates purchased from IonOptix (West-wood, MA, USA). Functionalized 3D-printed scaffolds were sterilized and adhered to the bottom on 48-well plates using sterile silicon grease as previously described, seeding each well with MC3T3 cells at a density of 40,000 cells/well. Once cells were attached, scaffolds were then transferred to 12-well plates fitted with carbon electrodes. Before electrical stimulation was applied, carbon electrodes were washed in 70% alcohol, dried, and further sterilized under UV irradiation for 1 h Electrical stimulation was then applied for 2 h per day at a voltage of 100 mV mm^{-1} and a frequency of 20 Hz, following previously reported methods [51, 52]. The electrical intensity effect on pre-osteoblast cell proliferation was preliminarily evaluated with varied voltages of 0, 50, 100, 200, 300, and 600 mV/mm. After each stimulation, the carbon electrodes were taken out, washed with 70% alcohol, dried, and stored in a sterilized environment. The proliferation of pre-osteoblasts on 3D-printed scaffolds was determined by MTS assay and the cellular morphologies were visualized using confocal microscopy after immunostaining as described above. The electrical field between the parallel carbon electrodes was simulated using MATLAB software (MathWorks, Natick, MA, USA) using the finite difference method as previously reported [53].

2.8. Osteogenic gene expression on 3D-printed scaffolds

2.8.1. Electrical stimulation and cell harvest—The effect of electrical stimulation on osteogenesis was determined by measuring bone marker gene mRNA expression using quantitative real-time PCR. To accomplish this, MC3T3 pre-osteoblasts were cultured in osteogenic α-MEM medium supplemented with 50 μg/mL ascorbic acid (AA) and 10 mM β-glycerophosphate (β-GP). For electrical stimulation groups, scaffolds with cells were stimulated for 2 h per day under voltage of 100 mV/mm and frequency of 20 Hz. At each time point, cells on 3D-printed scaffolds with or without exposure to electrical stimulation were harvested using trypsin and centrifuged at 3000 rpm for 10 min. Collected pre-osteoblasts were washed three times with sterilized ddH_2O and then lysed immediately.

2.8.2. RNA extraction and cDNA synthesis—RNA extractions were performed using the Aurum Total RNA Mini Kit (Bio-Rad, Herculues, CA, USA). The yield and purity of isolated RNA were quantified using a NanoDrop 2000 Spectrophotometer (Thermo Fisher Scientific, Waltham, MA, USA). First-strand cDNA was synthesized immediately through reverse transcription of isolated RNA using the iScript cDNA Synthesis Kit (Bio-Rad).

2.8.3. Real-time gene expression analysis—Quantitative reverse transcription-polymerase chain reaction (qRT-PCR) amplification was conducted using SsoAdvanced Universal SYBR Green Supermix (Bio-Rad, Germany) in conjunction with a CFX96 Touch Real-Time PCR Detection System (Bio-Rad, Germany) in triplicate. Two osteogenesis related genes, osteopontin (OPN) and runt-related transcription factor 2 (RUNX2), were analyzed using glyceraldehyde 3-phosphate dehydrogenase (GAPDH) as a reference gene. The 96-well PCR plates were directly ordered from Bio-Rad with mouse osteogenic specific primers incorporated within the wells. Gene expression levels of the messenger RNA (mRNA) for targeted genes were determined using the widely acknowledged comparative CT (threshold cycle values) method ($2^{-\Delta Ct}$) as previously reported [54]. Obtained relative quantification (RQ) data, which indicates the expression fold change relative to the GAPDH housekeeping gene, were averaged on three independent tests for cells on these 3D-printed scaffolds.

2.9. ALP activity and OCN content on 3D-printed scaffolds

2.9.1. Alkaline phosphatase (ALP) activity—MC3T3 cells were cultured in osteogenic α-MEM medium supplemented with 50 μg/mL AA and 10 mM β-GP on 3D-printed scaffolds as previously described. For electrical stimulation groups, cells were subjected to 100 mV mm^{-1} at 20 Hz for 2 h each day. After 14 days of co-culture, cells on 3D-printed scaffolds with or without electrical stimulation were harvested by trypsinization and centrifuge. To eliminate possible ethylenediaminetetraacetic acid (EDTA) residues from trypsin steps, harvested cells were thoroughly washed using ddH_2O 5 times, centrifuging after each wash. After counting to determine cell numbers using a cell counter, washed cells were lysed using 0.2% Triton X-100 at 4 °C overnight. The Triton to cell ratio were fixed at 0.5 mL solution per 1×10^4 cells for all groups. The intracellular alkaline phosphatase activity in cells harvested from varied 3D-printed scaffolds was determined using an alkaline phosphatase assay kit (QuantiChrome ^{TM}, BioAs-say Systems, Hayward, CA).

2.9.2. Osteocalcin (OCN) content—Pre-osteoblasts were seeded on 3D-printed scaffolds and cultured in an osteogenic α-MEM medium as previously described. After 21 days of culture, the osteocalcin content released by cells within the surrounding medium was tested using the mouse osteocalcin enzyme immunoassay quantitative kit (Alfa Aesar, Thermo Fisher Scientific) [55]. The absorbance at 450 nm for each sample test was read using a UV–vis absorbance microplate reader, calculating the final osteocalcin content from each group using a standard curve. At the same time, cell numbers on each type of 3D-printed scaffolds and treatment were counted after trypsinization. OCN content for each treatment group was normalized to the cell number within each well.

2.10. Statistical analysis

Results of assays are presented as the mean of several replicates, using the standard deviation as error bars. The statistical difference among treatment groups was determined using one-way analysis of variance (ANOVA). When an effect was statistically significant, a post hoc Tukey HSD test was conducted to determine the difference between groups. Comparisons of any two data groups that resulted in a $p\text{-value} < 0.05$ were marked as significantly different.

3. Results and discussion

3.1. Fabrication and characterization of ssDNA@CNT nanocomposites

The ssDNA was bound to CNT using ultra-sonication, as schematically demonstrated in Fig. 1a. After sonication, SEM imaging showed aggregated bundles of pure CNT (Fig. 2a) and independently separated tubes for ssDNA@CNT (Fig. 2b). TEM scoping demonstrated large aggregates with entangled formations when only CNTs were used, as presented in Fig. 2c. An enlarged view of single CNTs also showed closely stacked tubes, potentially aggregated by pi-pi stacking forces. For ssDNA@CNT, a well-dispersed homogeneous distribution with separated tubes was observed after sonication (Fig. 2d), with enlarged views showing the presence of single tube morphologies for the ssDNA@CNT with rough surfaces after binding with ssDNA chains, as indicated by arrows in Fig. 2d.

AFM was further conducted to confirm the dispersion ability of CNT and ssDNA@CNT. As displayed in Fig. 2e, pure CNT aggregated to form bundles with a height of 10–30 nm (Fig. S2a). After binding with ssDNA, ssDNA@CNT formed separate tubes (Fig. 2f) with heights around 2–10 nm (Fig. S2b).

After sonication, the ssDNA solution, CNT dispersions, and ssDNA@CNT dispersions were photographed at 0 h, 2 h, and 24 h to compare the degree of sedimentation. As can be seen in Fig. 2g, the ssDNA solution was clear and no aggregations were observed. The pure CNT solution, however, formed bundles easily and started to precipitate right after sonication. After binding with water-soluble ssDNA, the ssDNA@CNT nanocomposite displayed an enhanced ability to disperse within the solution, with no sedimentation observed even after 24 Hof stable storage. The zeta-potential test showed that pure CNTs owned slightly positive surface potential around 10 mV, while ssDNA@CNT showed strong negative surface with zeta potential tested to be −32 mV (Fig. 2H and Fig. S3). These results confirm that the ssDNA@CNT was truly negative and can be used for further adsorption onto the positively charged 3D-printed scaffolds surface.

The electrical conductivities for the CNT and ssDNA@CNT were tested both in solution and as a solid. At the same voltage, the current across CNT and ssDNA@CNT treatments at a concentration of 0.5 mg/mL were detected to be slightly different. The conductivity of ssDNA@CNT in solution (0.5 mg/mL) was slightly compromised compared to the pure CNTs (Fig. 2i). For conductivity tests on solid pellets, a similar trend was detected with slightly reduced conductivity for solid ssDNA@CNT pellets as compared to solid CNT (Fig. 2j). This reduction in conductivity may be the result of charge shielding that occurs when CNTs form complexes with ssDNA [56, 57]. Regardless of any observed differences, both the CNT and ssDNA@CNT pellets were found to be highly conductive, with conductivities higher than 200 S/m in solid-state.

3.2. Surface properties and cytotoxicity of 3D-printed scaffolds

3D PPF scaffolds were printed using a stereolithography technique and ammonolyzed in isopropyl alcohol containing hexamethylenediamine to produce a positively charged surface. Ammonolyzed 3D-printed scaffolds were functionalized with ssDNA, CNT, and ssDNA@CNT by soaking in respective solutions with dispersed components (Fig. 3a).

After functionalization, the appearance of each type of scaffold was photographed and presented in Fig. 3b. As can be seen in Fig. 3b, the original 3D-PPFA scaffolds as well as the 3D-PPFA-ssDNA scaffolds coated with ssDNA were clear in appearance. However, after functionalized with CNT bundles, the 3D-PPFA-CNT scaffolds showed dark dots randomly distributed around the surface, indicating a non-homogeneous coating of CNTs. In comparison, the 3D-PPFA-ssDNA@CNT scaffolds functionalized with ssDNA@CNT components showed a thick dark layer covering all the scaffold surfaces. This result indicates a homogeneous and large amount coating of ssDNA@CNT to 3D-printed scaffolds. A schematic illustration was presented under each type of scaffold to display each coating effect (Fig. 3b).

SEM scoping of scaffolds after functionalization confirmed what topographical differences observed between photographs were also present at the microscale. As can be seen in Fig. 3c, the un-functionalized 3D-PPFA scaffolds had fairly smooth surfaces. After functionalization with ssDNA, tinny aggregations were observed on the surface of 3D-PPFA-ssDNA scaffolds. After functionalization with CNT, large bundles were observed to be sparsely distributed on the surface of 3D-PPFA-CNT scaffolds, confirming their non-homogeneous distribution. However, after scaffolds were functionalized with ssDNA@CNT, a distributed thick layer of CNTs was observed covering the 3D-PPFA-ssDNA@CNT scaffolds, further confirming the homogeneous distribution of ssDNA@CNT.

The biocompatibility of functionalized scaffolds was evaluated using two methods. First, the scaffolds were placed in a transwell and co-cultured with cells to see the cytotoxicity of released components. As presented in Fig. 3d, live/dead staining showed most cells were alive, with no detectable differences among the wells exposed to scaffolds leaching media and the positive controls obtained from cell populations without exposure to scaffolds (Fig. 3e). Based on these results, a further step of direct culturing cells onto the surface of the scaffolds was conducted. As can be seen in Fig. 3f, most of the cells attached to the scaffolds' surface remained alive (green) with minimal evidence of cell death (red). Immunofluorescence imaging of the cells growing on scaffolds at day 1 (Fig. 3g) and day 7 (Fig. 3h) showed elevated proliferation of pre-osteoblast cells on these scaffolds, indicating favorable bio-compatibility of the scaffolds.

3.3. Osteoblast proliferation and focal adhesion development on 3D-printed scaffolds

To evaluate the proliferation capability of MC3T3 pre-osteoblast cells on scaffolds, the cell densities on scaffold treatment were determined by MTS after 1, 4, and 7 days of culture. Results showed that scaffolds functionalized with ssDNA (3D-PPFA-ssDNA) had slightly enhanced cell proliferation when compared with non-functionalized 3D-PPFA scaffolds, although the difference was not statistically significant (Fig. 4a). For scaffolds functionalized with CNT bundles, higher densities of cells were detected with significant differences observed after 7 days. For scaffolds functionalized with ssDNA@CNT, significantly higher densities of cells were observed at all time points including 1, 4, and 7 days of culture.

To observe the detailed cell morphology and cell-cell interactions on the surface of functionalized scaffolds, cells were immune-stained with rhodamine-phalloidin, anti-vinculin-FITC antibody, and DAPI and scoped using confocal microscopy. A clear trend of higher cell densities can be observed on 3D-PPFA-CNT and 3D-PPFA-ssDNA@CNT scaffolds, with comparably lower densities observed on non-functionalized 3D-PPFA and 3D-PPFA-ssDNA scaffolds (Fig. 4b and Fig. S6). Enlarged views with detailed cell components on each type of scaffolds were provided to better demonstrate the filament development and single vinculin morphologies (Fig. 4c).

Cells spread over a larger area when cultured on both 3D-PPFA-CNT and 3D-PPFA-ssDNA@CNT when compared with 3D-PPFA-ssDNA and non-functionalized 3D-PPFA scaffolds (Fig. 4d). Vinculin size demonstrated a similar trend, where vinculins were more developed on 3D-PPFA-CNT and 3D-PPFA-ssDNA@CNT scaffolds with the most robust vinculin expansion observed on the 3D-PPFA-ssDNA@CNT treatment (Fig. 4e). Furthermore, cells cultured on 3D-PPFA-ssDNA@CNT scaffolds displayed the lowest circulatory (Fig. 4f), indicating that the vinculins in cells on these scaffolds were largely stretched and elongated. All of these metrics point to superior adhesion and cell spreading on 3D-PPFA-ssDNA@CNT scaffolds. Vinculin expression, in particular, has been shown to be an important factor in the promotion of cell spreading on biomaterial implants [58], with focal adhesion itself playing a critical role in the regulation and anchoring of the extracellular matrix (ECM) [59, 60].

To visualize the cell-material interactions in each treatment, cells growing on the surface of all types of scaffolds were fixed, dehydrated, and viewed by SEM imaging. As can be seen from the results in Fig. 4g, cells on 3D-PPFA scaffolds showed limited filament development, while cells on 3D-PPFA-ssDNA scaffolds produced filaments between cells. For 3D-PPFA-CNT scaffolds, cells grew along with CNT bundles, with a detailed view showing the development of filaments surrounding CNT bundles is presented in the enlarged panel of Fig. 4g. On 3D-PPFA-ssDNA@CNT scaffolds, cells almost covered the entire scaffold surface, with robust filament formation observed at both the cell body and cell edge. The enlarged view showed clearly the distribution of single ssDNA@CNT tubes on the surface of the scaffolds, and cellular filaments were developed on these ssDNA@CNT tubes, as demonstrated in the enlarged panel from Fig. 4g. The ability of a ssDNA@CNT coated surface to support the development of the ECM could aid in tissue formation and help to ensure tissue-implant integration, a critical factor in the long-term success of bone implants that must contend with the constant remodeling of bone matrix to accurately replicate the complex architecture of bone [61].

3.4. Effect of electrical stimulation on pre-osteoblast behavior on 3D-printed scaffolds

There is a significant body of literature investigating the effect of electrical stimulation (ES) on bone growth in animal models as well as in a clinical setting, with notable benefit observed in the consolidation of fractures [62] and cortical thickening [63]. Electrical stimulation has also been shown to increase osteoblast proliferation when used in conjunction with conductive materials designed for use in bone tissue engineering applications, including titanium [64] and polypyrrole (PPy) [65], often in combination with heparin [66]. However, studies investigating the use of conductive carbon-based materials have been largely limited to carbon nanofibers (CNFs) [67] and carbon nanowalls [68] instead of carbon nanotubes (CNTs) due to concerns regarding their cytotoxicity and tendency to produce inflammatory responses in mammalian tissues [69].

Through combination with ssDNA, the results described here present a possible solution to the cytotoxicity problem inherent in CNT-based materials, while increasing the conductivity of synthetic 3D-printed scaffolds so that they can be used in conjunction with ES. We investigated the effect of electrical stimulation on the proliferation, morphology, and focal adhesion development of pre-osteoblasts growing on each type of functionalized 3D-printed scaffolds. After seeding, scaffolds with cells were stimulated using a C-Pace EP cell culture stimulator device with assortative 12-well plates and carbon electrodes (Fig. 5a and b). The electrical field was determined to be homogeneous in the specific region between the parallel carbon electrodes where the scaffolds were placed. An example calculation using voltage preset to 100 mV/mm is presented in Fig. 5c and d. These results show that a homogeneous electrical field intensity of 100 mV/mm was distributed across the scaffold area (Fig. 5c and d).

The influence of electrical intensity on pre-osteoblast cell proliferation was extensively evaluated with varied voltages of 0, 50, 100, 200, 300, and 600 mV/mm. After stimulation for 172 h, the cell numbers on each type of scaffolds were determined. As presented in Fig. 5e, a parabolic trend was found for the electrical voltage and proliferated cell numbers. When the electric field was increased to100 mV/mm, pre-osteoblast cell numbers were effectively stimulated on all four scaffold types when compared with their counterparts without electrical stimulation (0 mV/mm). However, electrical stimulation with high voltages of 200 and 300 mV/mm showed no stimulatory effects on cell proliferation. Instead, cell densities dropped after electrical stimulation a high voltage. When the voltage was set as high as 600 mV/mm, significantly lower cell densities were observed on all four scaffold types. This indicates that sufficiently high voltages either prohibit cell proliferation or may be lethal to a portion of the cell population. From these results, we estimate that the optimum voltage for MC3T3 pre-osteoblasts may be in the range of 50–200 mV/mm, with the results obtained from this study resulting from 100 mV/mm. This voltage range was commensurate with other studies that have used the MC3T3-E1 cell line, including those that have seen significant increases in osteogenesis related gene mRNA expression with 200 mV @ 100 Hz ES [28].

In this study, ES had a significant impact on MC3T3-E1 proliferation and cell density, regardless of the scaffold substrate on which the cells were grown (Fig. 5e). This result is consistent with other studies that have seen a drastic change in osteoblast proliferation on multiple substrate types [28, 70]. However, immunofluorescence imaging (Fig. 5f) in combination with MTS assays (Fig. 5g) showed that scaffolds functionalized with CNT bundles had significantly more cell proliferation after electrical stimulation, with an increase observed in the ssDNA@CNT treatment when compared with the non-conductive 3D-PPFA control. This result was also seen with respect to the cell density on ssDNA@CNT scaffolds after 7 days of ES (Fig. 5e), indicating that the conductivity and surface properties of this treatment likely acted synergistically under ES to improve cell viability.

To expand upon the observed increase in osteoblast proliferation on ssDNA@CNT scaffolds, detailed cell morphologies and cell-scaffold interactions under ES were investigated through immunestaining with rhodamine-phalloidin, anti-vinculin-FITC antibody, and DAPI (Fig. 5h–k and Fig. S7). As presented in Fig. 5h, the cells with the lowest focal adhesion circularity, *i.e.*, those that displayed the most elongated focal adhesions, were observed on the 3D-PPFA-ssDNA@CNT scaffolds Fig. 5h). In addition, significantly higher vinculin sizes were measured on 3D-PPFA-CNT and 3D-PPFA-ssDNA@CNT scaffolds when compared to the non-conductive 3D-PPFA control (Fig. 5i). Confocal immunofluorescence imaging similarly confirmed that there are higher densities of cells on the 3D-PPFA-CNT and 3D-PPFA-ssDNA@CNT, as compared with non-functionalized 3D-PPFA and 3D-PPFA-ssDNA scaffolds (Fig. 5j). Enlarged views with detailed immunofluorescence staining on each type of scaffolds demonstrated clearly robust filaments development and elongated vinculin morphologies on the 3D-PPFA-CNT and 3D-PPFA-ssDNA@CNT than the non-functionalized 3D-PPFA and 3D-PPFA-ssDNA scaffolds (Fig. 5k).

Unfortunately, the complexities inherent in studies that investigate the effect of ES in conjunction with conductive biomaterials on osteoblast growth limit their comparability. What is generally accepted is that osteoblasts, including the mouse pre-osteoblast M3CT3-E1 cell line used in this study, respond positively to ES under a variety of conditions, leading to an enhancement in cell proliferation, differentiation, and mineral formation [28, 71]. While the number of studies that measure osteoblast proliferation on surfaces with CNT in conjunction with ES is limited, our results are comparable to those using polylactic acid (PLA)/CNT composite, where an increase in proliferation was observed after stimulation with 200 mV @ 10 Hz for 2 days [72]. Similar results have been observed when PLA was combined with multiwalled carbon nanotubes (MWCNTs) when ES was applied at 50 μA, 100 μA, and 200 μA over 4 hrs for 6 days [73]. In this context, the robust cell-cell connections and cell-scaffold filaments observed on the 3D-PPFA-ssDNA@CNT scaffolds are additional evidence of their ability to support the expansion of the ECM in addition to improving osteoblast proliferation.

3.5. Osteogenic capacity of cells on 3D-printed scaffolds

Electrical stimulation (ES) has been shown to have a wide range of effects on the expression of osteogenic-markers, including notable increases in alkaline phosphatase (ALP), osteocalcin (OCN), bone morphogenic protein 2 (BMP2), and RUNX family transcription factor 2 (Runx2), even when stimulation is applied on non-conductive surfaces [65, 74–76]. In this study, we investigated the osteogenic capacity of pre-osteoblast cells on 3D-printed scaffolds with or without electrical stimulation. As presented in Fig. 6a, without electrical stimulation, ALP activity was detected to be significantly higher on 3D-PPFA-CNT and 3D-PPFA-ssDNA@CNT scaffolds than the 3D-PPFA-ssDNA and non-functionalized 3D-PPFA scaffolds. After electrical stimulations, ALP activity on all four types of 3D-printed scaffolds increased. However, the highest ALP activity was observed in pre-osteoblasts on 3D-PPFA-ssDNA@CNT scaffolds after electrical stimulation, resulting in significantly higher activity than the other three types of scaffolds. The OCN content was found to have a similar trend, with the highest OCN content detected on the 3D-PPFA-ssDNA@CNT scaffolds under both ES or non-ES conditions, both of which were significantly higher than the 3D-PPFA-CNT, 3D-PPFA-ssDNA and non-functionalized 3D-PPFA scaffolds (Fig. 6b).

The expression of other osteogenic markers in pre-osteoblasts growing on the 3D-printed scaffolds was analyzed using quantitative real-time PCR. As demonstrated in Fig. 6c and d, under non-ES condition, OPN and Runx2 gene expression were significantly higher in pre-osteoblasts on the functionalized 3D-PPFACNT and 3D-PPFA-ssDNA@CNT scaffolds than non-functionalized 3D-PPFA scaffolds. With electrical stimulation, the highest expression was detected in cells on the 3D-PPFA-ssDNA@CNT scaffolds and was found to be significantly higher than the other three types of scaffolds (Fig. 6c and d). These results indicate that the functionalization of ssDNA@CNT could effectively enhance the osteogenic capability of pre-osteoblast cells on the 3D-printed scaffolds.

The observed increase in the osteogenic-markers ALP, OCN, OPN, and Runx2 in pre-osteoblast cells grown on 3D-PPFA-ssDNA@CNT scaffolds under ES is evidence that, when localized in conjunction with a conductive substrate, electrical pulses can promote osteogenesis and mineral formation. While still poorly understood, one potential mechanism driving this effect could be electrical stimulation's induction of the Calcium/Calmodulin pathway. Electrical stimulation has been shown to induce MC3T3-E1 proliferation, an effect that has been attributed to the activation of voltage-gated calcium channels which lead to an increase in TGF-β1 mRNA levels [77]. TGF-β1 is an important regulator of osteogenesis, with direct interaction with the calcium-binding protein calmodulin, which in turn elicits responses from other proteins whose function has been linked to tissue mineralization [78, 79]. The activation of this pathway by ES and its effect on osteoblast growth, differentiation, and mineralization is an exciting possibility that is supported by our results and warrants further study.

4. Conclusions

In summary, we describe a simple one step method for the successful fabrication of 3D-printed scaffolds functionalized with carbon nanotubes (CNTs) for use in bone tissue engineering. The effect of CNT functionalization on the surface morphology and biocompatibility of scaffolds, as well as their ability to support pre-osteoblast cell attachment, proliferation, and osteogenic differentiation were examined. Our results showed that the functionalization of 3D-printed scaffolds with ssDNA bound CNT could significantly improve cell adhesion and spreading. Upon electrical stimulation (ES), robust cellular filaments and strong focal adhesions sites were developed around the cell edges. Additionally, enhanced ALP activity, OCN content, and the expression of other osteogenic makers further confirmed that cellular osteogenic differentiation was achieved on scaffolds functionalized with ssDNA@CNT components. These results clearly indicate that ssDNA@CNT functionalization negates the cytotoxicity of CNTs, enhances scaffold conductivity to improve compatibility with ES treatment, and effectively promotes pre-osteoblast cell proliferation and differentiation. These advantages make this functionalization route highly promising for tissue engineering applications, especially when employed in tissues that respond to exogenous electrical fields.

Supplementary Material

Refer to Web version on PubMed Central for supplementary material.

Acknowledgments

This work was supported by the National Institutes of Health Grant R01 AR56212.

References

[1]. Mironov V, Boland T, Trusk T, Forgacs G, Markwald RR, Organ printing: computer-aided jet-based 3D tissue engineering, Trends Biotechnol. 21 (2003) 157–161. [PubMed: 12679063]

[2]. Murphy SV, Atala A, 3D bioprinting of tissues and organs, Nat. Biotechnol 32 (2014) 773. [PubMed: 25093879]

[3]. Bose S, Vahabzadeh S, Bandyopadhyay A, Bone tissue engineering using 3D printing, Mater. Today 16 (2013) 496–504.

[4]. Grayson ACR, Cima MJ, Langer R, Size and temperature effects on poly (lactic-co-glycolic acid) degradation and microreservoir device performance, Biomaterials 26 (2005) 2137–2145. [PubMed: 15576189]

[5]. Lasprilla AJ, Martinez GA, Lunelli BH, Jardini AL, Maciel Filho R, Poly-lactic acid synthesis for application in biomedical devices—a review, Biotechnol. Adv 30 (2012) 321–328. [PubMed: 21756992]

[6]. Thibault RA, Scott Baggett L, Mikos AG, Kasper FK, Osteogenic differentiation of mesenchymal stem cells on pregenerated extracellular matrix scaffolds in the absence of osteogenic cell culture supplements, Tissue Eng. Part A 16 (2009) 431–440.

[7]. Henry MG, Cai L, Liu XF, Zhang L, Dong JY, Chen L, Wang ZQ, Wang SF, Roles of hydroxyapatite allocation and microgroove dimension in promoting preosteoblastic cell functions on photocured polymer nanocomposites through nuclear distribution and alignment, Langmuir 31 (2015) 2851–2860. [PubMed: 25710252]

[8]. Cai L, Foster CJ, Liu XF, Wang SF, Enhanced bone cell functions on poly(epsilon-caprolactone) triacrylate networks grafted with polyhedral oligomeric silsesquioxane nanocages, Polymer 55 (2014) 3836–3845.

[9]. Kasper FK, Tanahashi K, Fisher JP, Mikos AG, Synthesis of poly (propylene fumarate), Nat. Protoc 4 (2009) 518–525. [PubMed: 19325548]

[10]. Fisher JP, Holland TA, Dean D, Engel PS, Mikos AG, Synthesis and properties of photocross-linked poly(propylene fumarate) scaffolds, J. Biomater. Sci. Polym. Ed 12 (2001) 673–687. [PubMed: 11556743]

[11]. Liu X, Miller AL, Xu H, Waletzki BE, Lu L, Injectable catalyst-free poly (Propylene Fumarate) system cross-linked by strain promoted alkyne-azide cycloaddition click chemistry for spine defect filling, Biomacromolecules 20 (2019) 3352–3365. [PubMed: 31398020]

[12]. Olthof MGL, Kempen DHR, Herrick JL, Yaszemski MJ, Dhert WJA, Lu L, Effect of different sustained bone morphogenetic protein-2 release kinetics on bone formation in poly(propylene fumarate) scaffolds, J. Biomed. Mater. Res. Part B 106 (2018) 477–487.

[13]. Lee K−W, Wang S, Fox BC, Ritman EL, Yaszemski MJ, Lu L, Poly (propylene fumarate) bone tissue engineering scaffold fabrication using stereolithography: effects of resin formulations and laser parameters, Biomacromolecules 8 (2007) 1077–1084. [PubMed: 17326677]

[14]. Dadsetan M, Guda T, Runge MB, Mijares D, LeGeros RZ, LeGeros JP, Silliman DT, Lu L, Wenke JC, Baer PRB, Effect of calcium phosphate coating and rhBMP-2 on bone regeneration in rabbit calvaria using poly (propylene fumarate) scaffolds, Acta Biomater. 18 (2015) 9–20. [PubMed: 25575855]

[15]. Oprych KM, Whitby RL, Mikhalovsky SV, Tomlins P, Adu J, Repairing peripheral nerves: is there a role for carbon nanotubes? Adv. Healthc. Mater 5 (2016) 1253–1271. [PubMed: 27027923]

[16]. Shin SR, Farzad R, Tamayol A, Manoharan V, Mostafalu P, Zhang YS, Akbari M, Jung SM, Kim D, Comotto M, A Bioactive Carbon Nanotube-Based Ink for Printing 2D and 3D Flexible Electronics, Adv. Mater 28 (2016) 3280–3289. [PubMed: 26915715]

[17]. Liu X, Kim JC, Miller AL, Waletzki BE, Lu L, Electrically conductive nanocomposite hydrogels embedded with functionalized carbon nanotubes for spinal cord injury, New J. Chem 42 (2018) 17671–17681.

[18]. Ramón-Azcón J, Ahadian S, Estili M, Liang X, Ostrovidov S, Kaji H, Shiku H, Ramalingam M, Nakajima K, Sakka Y, Dielectrophoretically aligned carbon nanotubes to control electrical and mechanical properties of hydrogels to fabricate contractile muscle myofibers, Adv. Mater 25 (2013) 4028–4034. [PubMed: 23798469]

[19]. Cha C, Shin SR, Annabi N, Dokmeci MR, Khademhosseini A, Carbon-based nanomaterials: multifunctional materials for biomedical engineering, ACS Nano 7 (2013) 2891–2897. [PubMed: 23560817]

[20]. Zhang YS, Khademhosseini A, Advances in engineering hydrogels, Science (2017) 356 eaaf3627.

[21]. Cellot G, Cilia E, Cipollone S, Rancic V, Sucapane A, Giordani S, Gambazzi L, Markram H, Grandolfo M, Scaini D, Carbon nanotubes might improve neuronal performance by favouring electrical shortcuts, Nat. Nanotechnol 4 (2009) 126–133. [PubMed: 19197316]

[22]. Cellot G, Toma FM, Varley ZK, Laishram J, Villari A, Quintana M, Cipollone S, Prato M, Ballerini L, Carbon nanotube scaffolds tune synaptic strength in cultured neural circuits: novel frontiers in nanomaterial-tissue interactions, J. Neurosci 31 (2011) 12945–12953. [PubMed: 21900573]

[23]. Liu X, Miller II AL, Park S, Waletzki BE, Terzic A, Yaszemski MJ, Lu L, Covalent crosslinking of graphene oxide and carbon nanotube into hydrogels enhances nerve cell responses, J. Mater. Chem B 4 (2016) 6930–6941.

[24]. Fabbro A, Bosi S, Ballerini L, Prato M, Carbon nanotubes: artificial nanomaterials to engineer single neurons and neuronal networks, ACS Chem. Neurosci 3 (2012) 611–618. [PubMed: 22896805]

[25]. Huang YJ, Wu HC, Tai NH, Wang TW, Carbon nanotube rope with electrical stimulation promotes the differentiation and maturity of neural stem cells, Small 8 (2012) 2869–2877. [PubMed: 22753249]

[26]. Liu X, Miller AL, Park S, Waletzki BE, Zhou Z, Terzic A, Lu L, Functionalized carbon nanotube and graphene oxide embedded electrically conductive hydrogel synergistically stimulates nerve cell differentiation, ACS Appl. Mater. Interfaces 9 (2017) 14677–14690. [PubMed: 28406608]

[27]. Jin G−Z, Kim M, Shin US, Kim H−W, Neurite outgrowth of dorsal root ganglia neurons is enhanced on aligned nanofibrous biopolymer scaffold with carbon nanotube coating, Neurosci. Lett 501 (2011) 10–14. [PubMed: 21723372]

[28]. Wang Y, Cui H, Wu Z, Wu N, Wang Z, Chen X, Wei Y, Zhang P, Modulation of osteogenesis in MC3T3-E1 cells by different frequency electrical stimulation, PLoS One 11 (2016) e0154924.

[29]. Leppik L, Zhihua H, Mobini S, Parameswaran VT, Eischen-Loges M, Slavici A, Helbing J, Pindur L, Oliveira KM, Bhavsar MB, Combining electrical stimulation and tissue engineering to treat large bone defects in a rat model, Sci. Rep.-Uk 8 (2018) 6307.

[30]. Gao C, Feng P, Peng S, Shuai C, Carbon nanotube, graphene and boron nitride nanotube reinforced bioactive ceramics for bone repair, Acta Biomater. 61 (2017) 1–20. [PubMed: 28501710]

[31]. Ormsby R, McNally T, O'Hare P, Burke G, Mitchell C, Dunne N, Fatigue and biocompatibility properties of a poly(methyl methacrylate) bone cement with multi-walled carbon nanotubes, Acta Biomater. 8 (2012) 1201–1212. [PubMed: 22023747]

[32]. Fatemi SM, Foroutan M, Recent developments concerning the dispersion of carbon nanotubes in surfactant/polymer systems by MD simulation, J. Nanostruct. Chem 6 (2016) 29–40.

[33]. Koh B, Cheng W, Mechanisms of carbon nanotube aggregation and the reversion of carbon nanotube aggregates in aqueous medium, Langmuir 30 (2014) 10899–10909. [PubMed: 25144606]

[34]. Kharissova OV, Kharisov BI, de Casas Ortiz EG, Dispersion of carbon nanotubes in water and non-aqueous solvents, RSC Adv. 3 (2013) 24 812–24 852.

[35]. Heister E, Lamprecht C, Neves V, Tîlmaciu C, Datas L, Flahaut E, Soula B, Hinterdorfer P, Coley HM, Silva SRP, Higher dispersion efficacy of functionalized carbon nanotubes in chemical and biological environments, ACS Nano 4 (2010) 2615–2626. [PubMed: 20380453]

[36]. Liu Z, Sun X, Nakayama-Ratchford N, Dai H, Supramolecular chemistry on water-soluble carbon nanotubes for drug loading and delivery, ACS Nano 1 (2007) 50–56. [PubMed: 19203129]

[37]. Liu Z, Cai W, He L, Nakayama N, Chen K, Sun X, Chen X, Dai H, In vivo biodistribution and highly efficient tumour targeting of carbon nanotubes in mice, Nat. Nanotechnol 2 (2007) 47. [PubMed: 18654207]

[38]. Li Z, Wu Z, Li K, The high dispersion of DNA–multiwalled carbon nanotubes and their properties, Anal. Biochem 387 (2009) 267–270. [PubMed: 19454222]

[39]. Dolash BD, Lahiji RR, Zemlyanov DY, Drachev VP, Reifenberger R, Bergstrom DE, Sonication mediated covalent cross-linking of DNA to single-walled carbon nanotubes, Chem. Phys 413 (2013) 11–19.

[40]. Hu C, Zhang Y, Bao G, Zhang Y, Liu M, Wang ZL, DNA functionalized single-walled carbon nanotubes for electrochemical detection, J. Phys. Chem. B 109 (2005) 20072–20076. [PubMed: 16853595]

[41]. Zinchenko A, Taki Y, Sergeyev V, Murata S, DNA-assisted solubilization of carbon nanotubes and construction of DNA-MWCNT cross-linked hybrid hydrogels, Nanomaterials 5 (2015) 270–283. [PubMed: 28347011]

[42]. Zheng M, Jagota A, Semke ED, Diner BA, McLean RS, Lustig SR, Richardson RE, Tassi NG, DNA-assisted dispersion and separation of carbon nanotubes, Nat. Mater 2 (2003) 338. [PubMed: 12692536]

[43]. Premkumar T, Mezzenga R, Geckeler KE, Carbon nanotubes in the liquid phase: addressing the issue of dispersion, Small 8 (2012) 1299–1313. [PubMed: 22431156]

[44]. Malarkey EB, Fisher KA, Bekyarova E, Liu W, Haddon RC, Parpura V, Conductive single-walled carbon nanotube substrates modulate neuronal growth, Nano Lett. 9 (2008) 264–268.

[45]. Schipper ML, Nakayama-Ratchford N, Davis CR, Kam NWS, Chu P, Liu Z, Sun X, Dai H, Gambhir SS, A pilot toxicology study of single-walled carbon nanotubes in a small sample of mice, Nat. Nanotechnol 3 (2008) 216–221. [PubMed: 18654506]

[46]. Tang S, Tang Y, Zhong L, Murat K, Asan G, Yu J, Jian R, Wang C, Zhou P, Short-and long-term toxicities of multi-walled carbon nanotubes in vivo and in vitro, J. Appl. Toxicol 32 (2012) 900–912. [PubMed: 22760929]

[47]. Liu X, Miller II AL, Waletzki BE, Yaszemski MJ, Lu L, Novel biodegradable poly (propylene fumarate)-co-poly (L-lactic acid) porous scaffolds fabricated by phase separation for tissue engineering applications, RSC Adv. 5 (2015) 21301–21309. [PubMed: 26989483]

[48]. Park S, Terzic A, Quaternary structure of KATP channel SUR2A nucleotide binding domains resolved by synchrotron radiation X-ray scattering, J. Struct. Biol 169 (2010) 243–251. [PubMed: 19919849]

[49]. Kim D, Kim DW, Hong WG, Coskun A, Graphene/ZIF-8 composites with tunable hierarchical porosity and electrical conductivity, J. Mater. Chem. A 4 (2016) 7710–7717.

[50]. Liu X, Miller AL, Park S, George M, Waletzki BE, Xu H, Terzic A, Lu L, Two-dimensional black phosphorus and graphene oxide nanosheets synergistically enhance cell proliferation and osteogenesis on 3D-printed scaffolds, ACS Appl. Mater. Interfaces 11 (2019) 23558–23572. [PubMed: 31199116]

[51]. Prabhakaran MP, Ghasemi-Mobarakeh L, Jin G, Ramakrishna S, Electrospun conducting polymer nanofibers and electrical stimulation of nerve stem cells, J. Biosci. Bioeng 112 (2011) 501–507. [PubMed: 21813321]

[52]. Qi F, Wang Y, Ma T, Zhu S, Zeng W, Hu X, Liu Z, Huang J, Luo Z, Electrical regulation of olfactory ensheathing cells using conductive polypyrrole/chitosan polymers, Biomaterials 34 (2013) 1799–1809. [PubMed: 23228424]

[53]. Sadiku MN, Elements of Electromagnetic, Chap. 14, The Finite Difference Method, fourth ed., Oxford university press, 2007.

[54]. Livak KJ, Schmittgen TD, Analysis of relative gene expression data using real–time quantitative PCR and the 2 −CT method, Methods 25 (2001) 402–408. [PubMed: 11846609]

[55]. Chiu R, Ma T, Smith RL, Goodman SB, Polymethylmethacrylate particles inhibit osteoblastic differentiation of MC3T3-E1 osteoprogenitor cells, J. Orthop. Res 26 (2008) 932–936. [PubMed: 18302244]

[56]. Schroeder V, Savagatrup S, He M, Lin S, Swager TM, Carbon nanotube chemical sensors, Chem. Rev 119 (2018) 599–663. [PubMed: 30226055]

[57]. Venkataraman A, Amadi EV, Chen Y, Papadopoulos C, Carbon Nanotube Assembly and Integration for Applications, Nanoscale Res. Lett 14 (2019) 1–47. [PubMed: 30607516]

[58]. Woodruff MA, Jones P, Farrar D, Grant DM, Scotchford CA, Human osteoblast cell spreading and vinculin expression upon biomaterial surfaces, J. Mol. Histol 38 (2007) 4 91–4 99.

[59]. Dugina V, Fontao L, Chaponnier C, Vasiliev J, Gabbiani G, Focal adhesion features during myofibroblastic differentiation are controlled by intracellular and extracellular factors, J. Cell. Sci 114 (2001) 3285–3296. [PubMed: 11591817]

[60]. Diener A, Nebe B, Lüthen F, Becker P, Beck U, Neumann HG, Rychly J, Control of focal adhesion dynamics by material surface characteristics, Biomaterials 26 (2005) 383–392. [PubMed: 15275812]

[61]. Khan Y, Yaszemski MJ, Mikos AG, Laurencin CT, Tissue engineering of bone: material and matrix considerations, J Bone Joint Surg Am 90a (2008) 36–42.

[62]. Shayesteh YS, Eslami B, Dehghan MM, Vaziri H, Alikhassi M, Mangoli A, Khojasteh A, The effect of a constant electrical field on osseointegration after immediate implantation in dog mandibles: a preliminary study, J. Prosthodont 16 (2007) 337–342. [PubMed: 17559534]

[63]. Schindler K, Elger CE, Lehnertz K, Changes of EEG synchronization during low-frequency electric stimulation of the seizure onset zone, Epilepsy Res. 77 (2007) 108–119. [PubMed: 17980557]

[64]. Ercan B, Webster TJ, Greater osteoblast proliferation on anodized nanotubular titanium upon electrical stimulation, Int. J. Nanomed 3 (2008) 477.

[65]. Meng S, Zhang Z, Rouabhia M, Accelerated osteoblast mineralization on a conductive substrate by multiple electrical stimulation, J. Bone Miner. Metab 29 (2011) 535–544. [PubMed: 21327884]

[66]. Meng S, Rouabhia M, Zhang Z, Electrical stimulation modulates osteoblast proliferation and bone protein production through heparin-bioactivated conductive scaffolds, Bioelectromagnetics 34 (2013) 189–199. [PubMed: 23124591]

[67]. Samadian H, Mobasheri H, Hasanpour S, Ai J, Azamie M, Faridi-Majidi R, Electro-conductive carbon nanofibers as the promising interfacial biomaterials for bone tissue engineering, J. Mol. Liq 298 (2020) 112021.

[68]. Ichikawa T, Tanaka S, Kondo H, Ishikawa K, Tsutsumi T, Sekine M, Hori M, Effect of electrical stimulation on proliferation and bone-formation by osteoblast-like cells cultured on carbon nanowalls scaffolds, Appl. Phys. Express 12 (2019) 025006.

[69]. Shvedova A, Kisin E, Porter D, Schulte P, Kagan V, Fadeel B, Castranova V, Mechanisms of pulmonary toxicity and medical applications of carbon nanotubes: two faces of Janus? Pharmacol. Ther 121 (2009) 192–204. [PubMed: 19103221]

[70]. Brighton CT, Okereke E, Pollack SR, Clark CC In vitro bone-cell response to a capacitively coupled electrical field. The role of field strength, pulse pattern, and duty cycle. Clin. Orthop. Relat. R1992:255–62.

[71]. Yonemori K, Matsunaga S, Ishidou Y, Maeda S, Yoshida H, Early effects of electrical stimulation on osteogenesis, Bone 19 (1996) 173–180. [PubMed: 8853862]

[72]. Supronowicz P, Ajayan P, Ullmann K, Arulanandam B, Metzger D, Bizios R, Novel current-conducting composite substrates for exposing osteoblasts to alternating current stimulation, J. Biomed. Mater. Res 59 (2002) 499–506. [PubMed: 11774308]

[73]. Shao S, Zhou S, Li L, Li J, Luo C, Wang J, Li X, Weng J, Osteoblast function on electrically conductive electrospun PLA/MWCNTs nanofibers, Biomaterials 32 (2011) 2821–2833. [PubMed: 21292320]

[74]. Torricelli P, Fini M, Giavaresi G, Botter R, Beruto D, Giardino R, Biomimetic PMMA-based bone substitutes: a comparative in vitro evaluation of the effects of pulsed electromagnetic field exposure, J. Biomed. Mater. Res. Part A 64 (2003) 182–188.

[75]. Wang Z, Clark CC, Brighton CT, Up-regulation of bone morphogenetic proteins in cultured murine bone cells with use of specific electric fields, JBJS 88 (2006) 1053–1065.

[76]. Wiesmann H, Joos U, Meyer U, Biological and biophysical principles in extracorporal bone tissue engineering: part II, Int. J. Oral Maxillofac. Surg 33 (2004) 523–530. [PubMed: 15308249]

[77]. Zhuang H, Wang W, Seldes RM, Tahernia AD, Fan H, Brighton CT, Electrical stimulation induces the level of TGF-β1 mRNA in osteoblastic cells by a mechanism involving calcium/calmodulin pathway, Biochem. Biophys. Res. Commun 237 (1997) 225–229. [PubMed: 9268690]

[78]. Zayzafoon M, Calcium/calmodulin signaling controls osteoblast growth and differentiation, J. Cell Biochem 97 (2006) 56–70. [PubMed: 16229015]

[79]. Oshima S, Watanabe M, Elevated expression of calcineurin subunits during active mineralization of developing mouse molar teeth, Eur. J. Oral Sci 120 (2012) 386–394. [PubMed: 22984995]

Statement of Significance

Three-dimensional (3D) printing is a promising technology for tissue engineering. However, 3D-printing methods have limited ability to produce desired features or electrochemical properties in support of robust cell behavior. To address this deficiency, the current study proposed an integrated, one-step method to increase the cytocompatibility of 3D-printed scaffolds through functionalization leveraging conductive carbon nanotubes (CNTs). This fast and facile functionalization resulted in a homogenous and non-toxic coating of CNTs to the surface, which significantly improved the adhesion, proliferation, and differentiation of cells on the 3D-printed scaffolds.

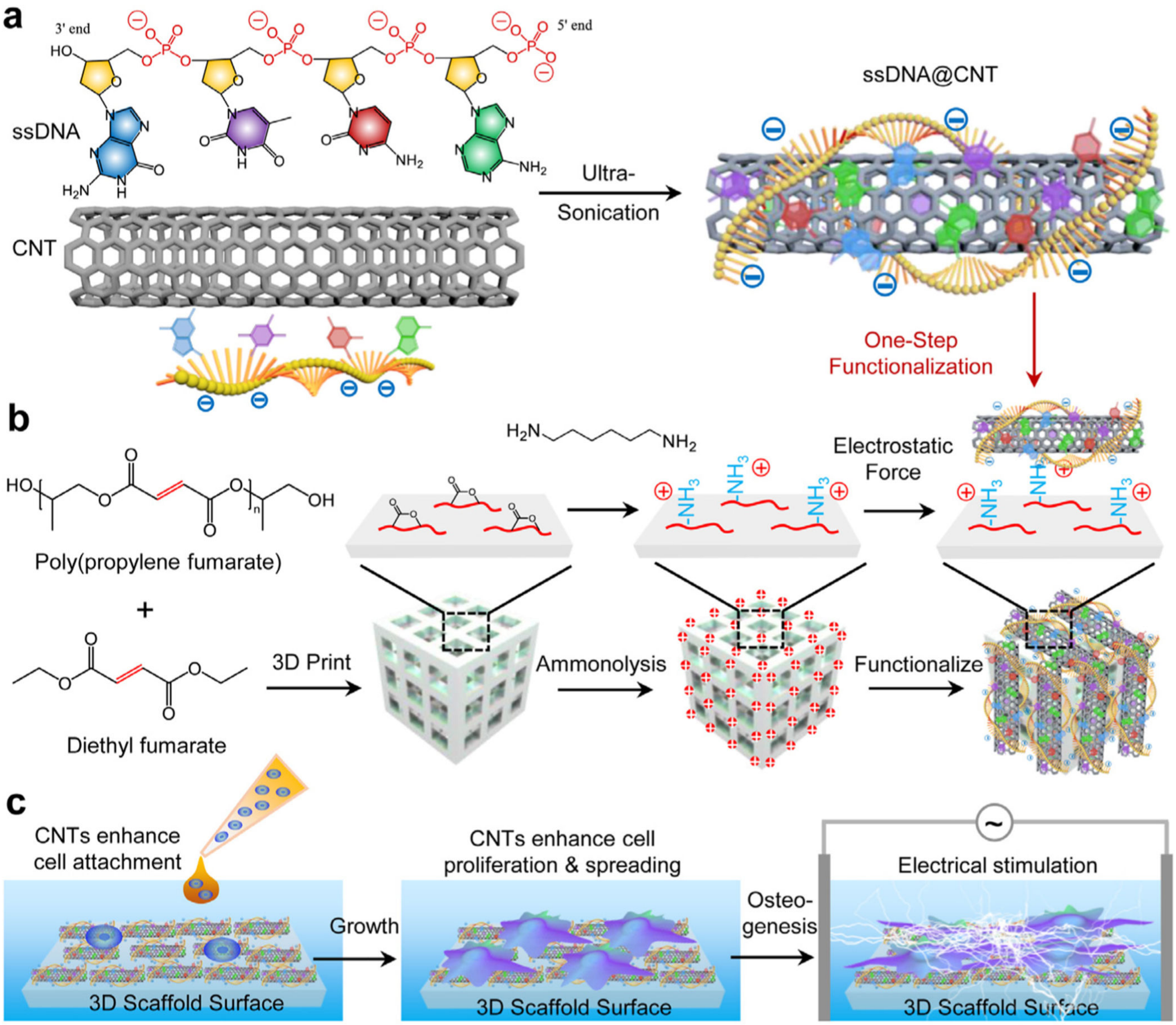

Fig. 1.

Schematic illustrations. a) Fabrication of ssDNA@CNT by ultra-sonication of ssDNA and CNTs. b) 3D scaffold–printing and subsequent ammonolysis and functionalization by ssDNA@CNT through electrostatic forces between positively charged 3D scaffold surfaces and negatively charged ssDNA@CNT composites. c) Enhanced cell proliferation and osteogenesis under electrical stimulation in the presence of ssDNA@CNTs.

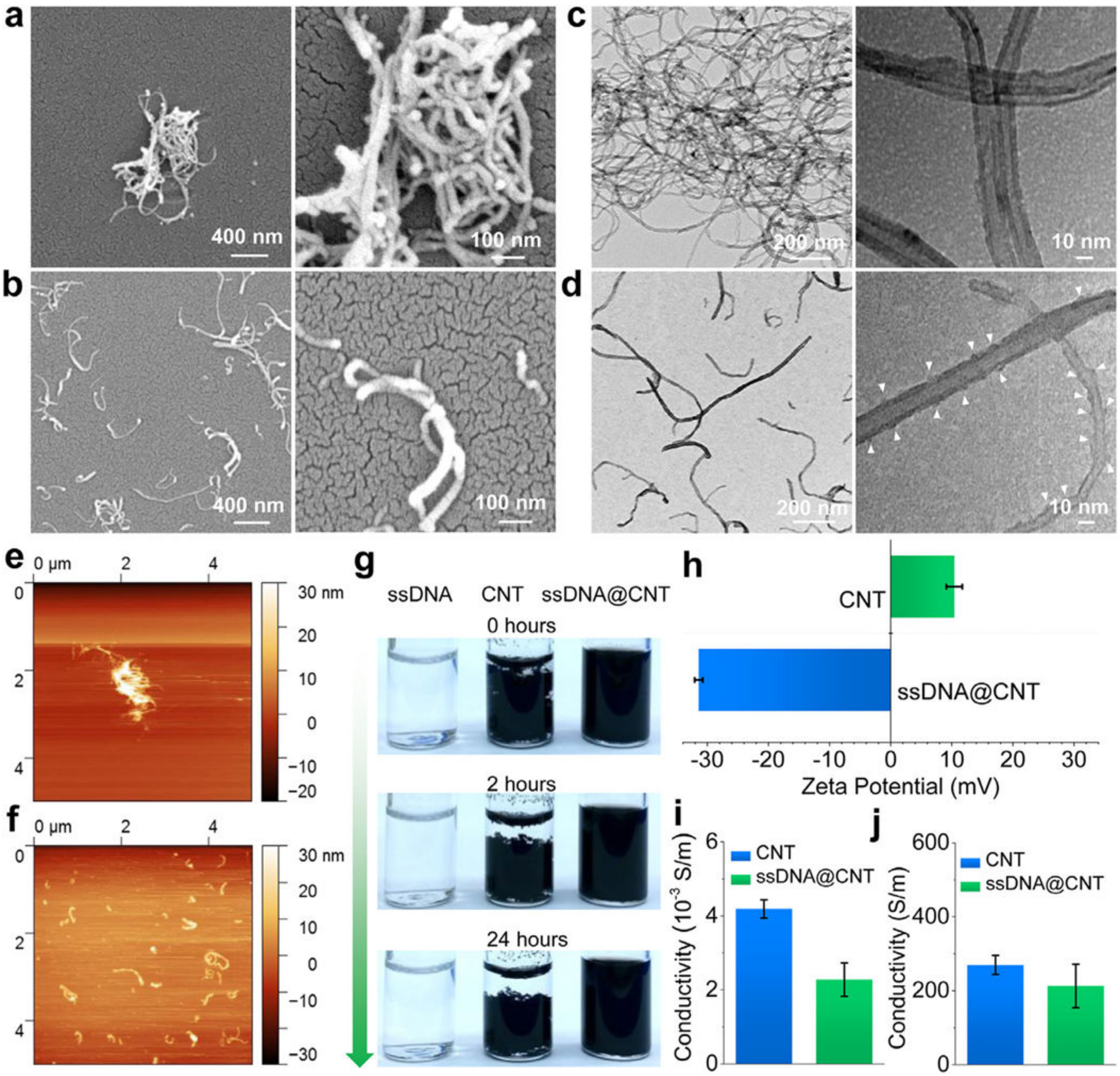

Fig. 2.

Characterization of ssDNA@CNT nanocomposite. SEM characterization of a) CNT and b) ssDNA@CNT nanocomposite. TEM images of c) CNT and d) ssDNA@CNT nanocomposite. AFM mapping of e) CNT and f) ssDNA@CNT nanocomposite. g) Photographs of ssDNA, CNT, and ssDNA@CNT solutions at different times after sonication. h) Zeta potential of CNT and ssDNA@CNT nanocomposites tested by DLS. i) Conductivity tested for CNT and ssDNA@CNT at a concentration of 0.5 mg/mL. j) Conductivities of solid CNT and ssDNA@CNT pellets.

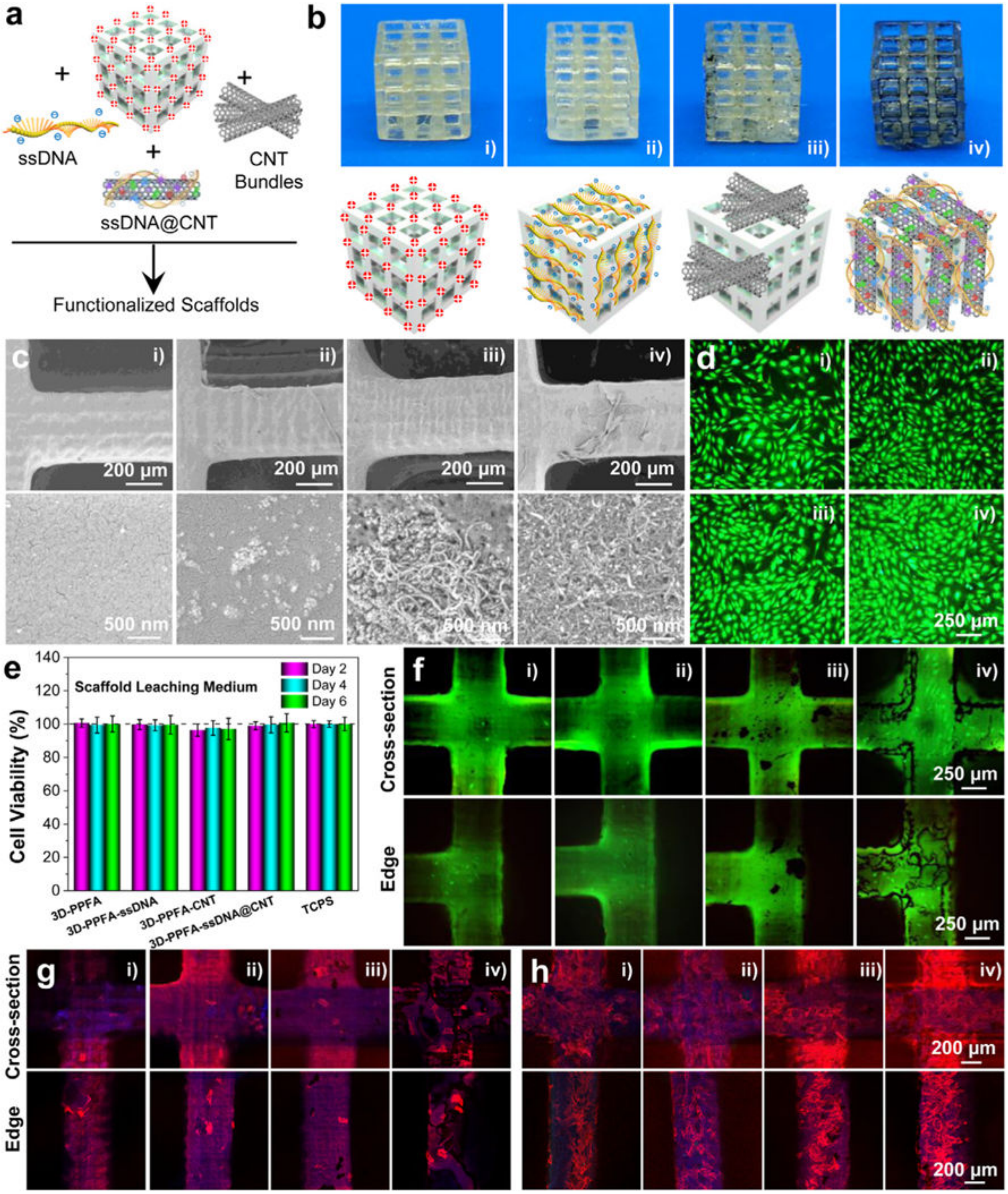

Fig. 3.

3D-printed scaffold fabrication and characterization. a) Schematic demonstration and b) photographs of 3D-PPFA scaffolds before and after functionalization with ssDNA, CNT, and ssDNA@CNT materials. c) SEM images of 3D-PPFA scaffolds before and after functionalization. d) Live/dead imaging and e) cell viability of MC3T3 pre-osteoblast cells after exposure to the scaffold leaching medium. f) Live/dead imaging of MC3T3 cells after direct seeding onto scaffold surfaces. Confocal immunofluorescence imaging of MC3T3 cells at g) 1 day and h) 7 days post-seeding on the scaffolds (red: F-actin; blue: cell nuclei).

(i: 3D-PPFA; ii: 3D-PPFA-ssDNA; iii: 3D-PPFA-CNT; iv: 3D-PPFA-ssDNA@CNT). (For interpretation of the references to color in this figure legend, the reader is referred to the web version of this article.)

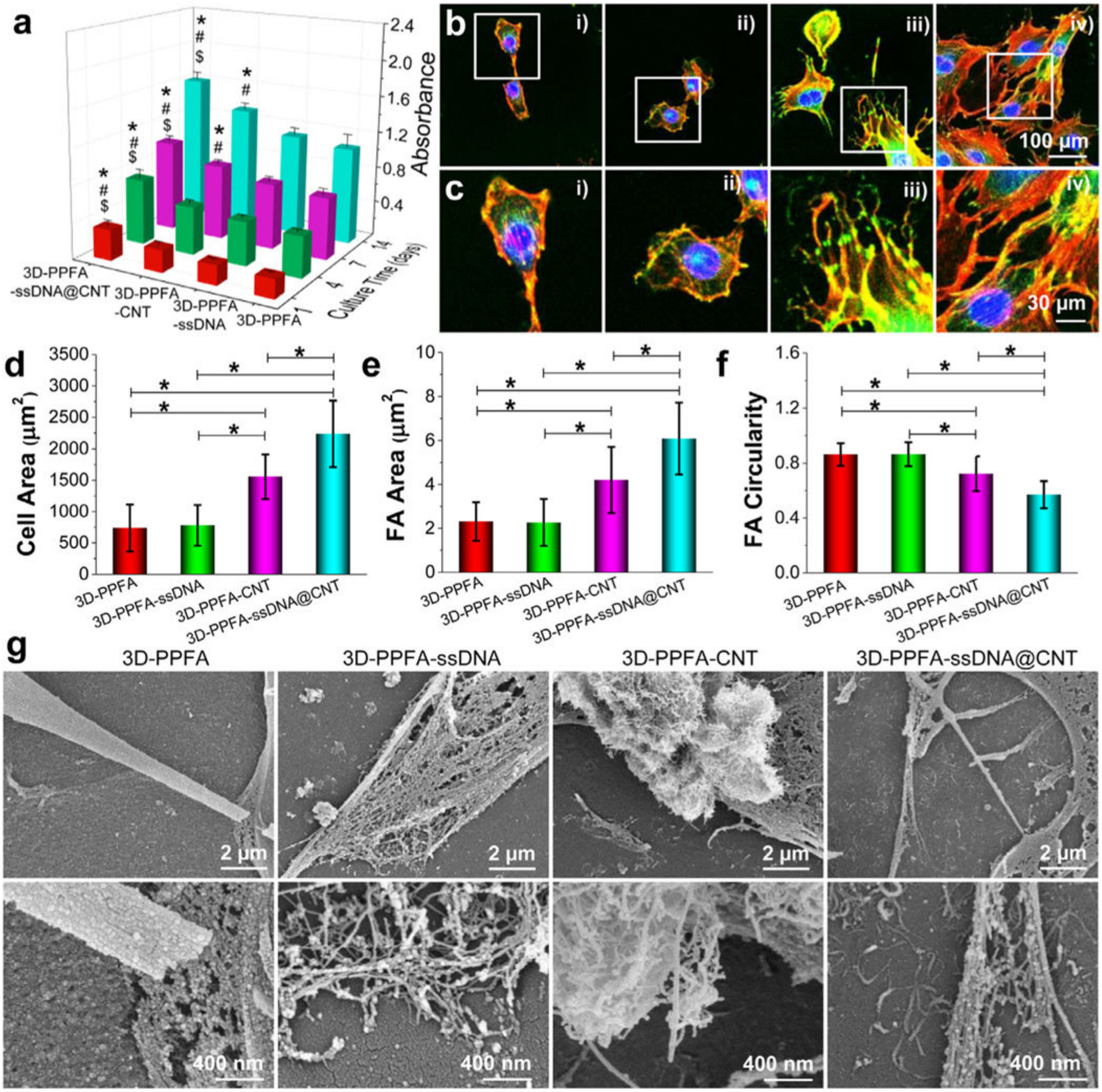

Fig. 4.

Cell-scaffold interactions. a) Proliferation of MC3T3 pre-osteoblast cells cultured on various 3D scaffolds. b) Confocal immunofluorescence imaging of filaments and focal adhesion development in single cells on scaffolds (Red: F-Actin; Green: Vinculin; Blue: Nuclei). i): 3D-PPFA; ii): 3D-PPFA-ssDNA; iii): 3D-PPFA-CNT; iv): 3D-PPFA-ssDNA@CNT scaffolds. c) Enlarged detailed view of cell and focal adhesion morphologies. d) Cell spreading area, e) focal adhesion area, and f) focal adhesion circularity of cells on scaffolds (*: $p < 0.05$). g) SEM images showing cell-materials interactions in each treatment group.

(For interpretation of the references to color in this figure legend, the reader is referred to the web version of this article.)

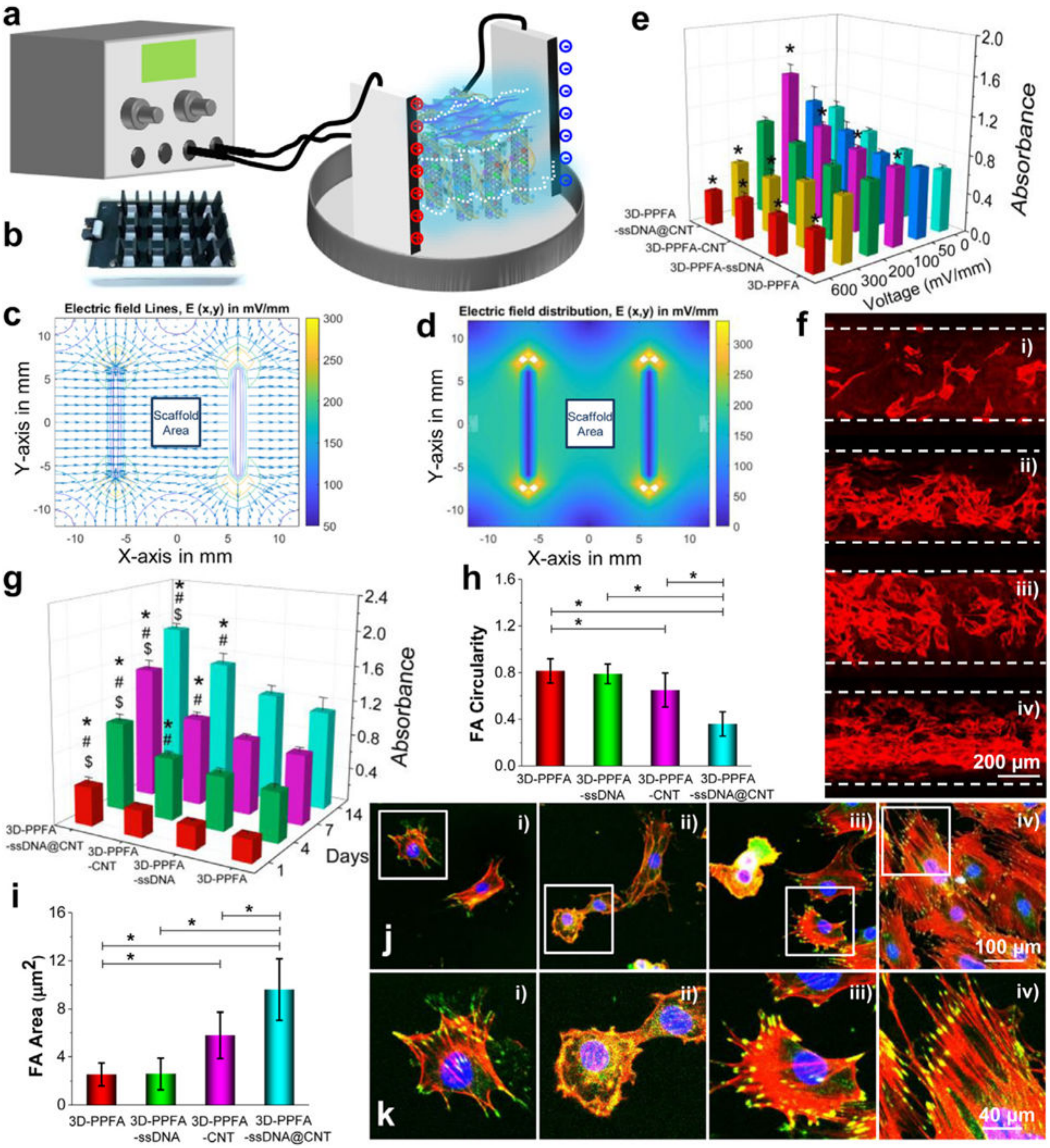

Fig. 5.

Electrical stimulation. a) Schematic demonstration and b) the plates used for electrical stimulation of MC3T3 pre-osteoblast cells cultured on various 3D scaffolds. c) Electrical filed line simulation and d) electrical field distribution surrounding the scaffold area. e) Relative cell numbers in response to varied stimulation voltages. The values were normalized to that of the 3D-PPFA non-ES (0 mV) group (set as 100). *: $p < 0.05$ compared to the same type of scaffolds without ES treatment (0 mV). f) Immunofluorescence images of cells cultured on 3D-PPFA, 3D-PPFA-ssDNA, 3D-PPFA-CNT, and 3D-PPFA-ssDNA@CNT scaffolds. (Red: F-Actin). g) Cell numbers detected by MTS on the 3D-printed scaffolds. (*: $p < 0.05$ compared to 3D-PPFA group within the same time point; #: $p < 0.05$ compared to 3D-PPFA-ssDNA group within the same time point; &: $p < 0.05$ compared to 3D-PPFA-CNT group within the same time point). h) Focal adhesion circularity and i) focal adhesion area of pre-osteoblast cells growing on the scaffolds after electrical stimulation (*: $p < 0.05$). j) Confocal imaging and k) enlarged views of filaments and focal adhesion development in single cells cultured on 3D scaffolds after electrical stimulation (Red: F-Actin; Green: Vinculin; Blue: Nuclei). i): 3D-PPFA; ii): 3D-PPFA-ssDNA; iii): 3D-PPFA-CNT; iv): 3D-PPFA-ssDNA@CNT scaffolds. (For interpretation of the references to color in this figure legend, the reader is referred to the web version of this article.)

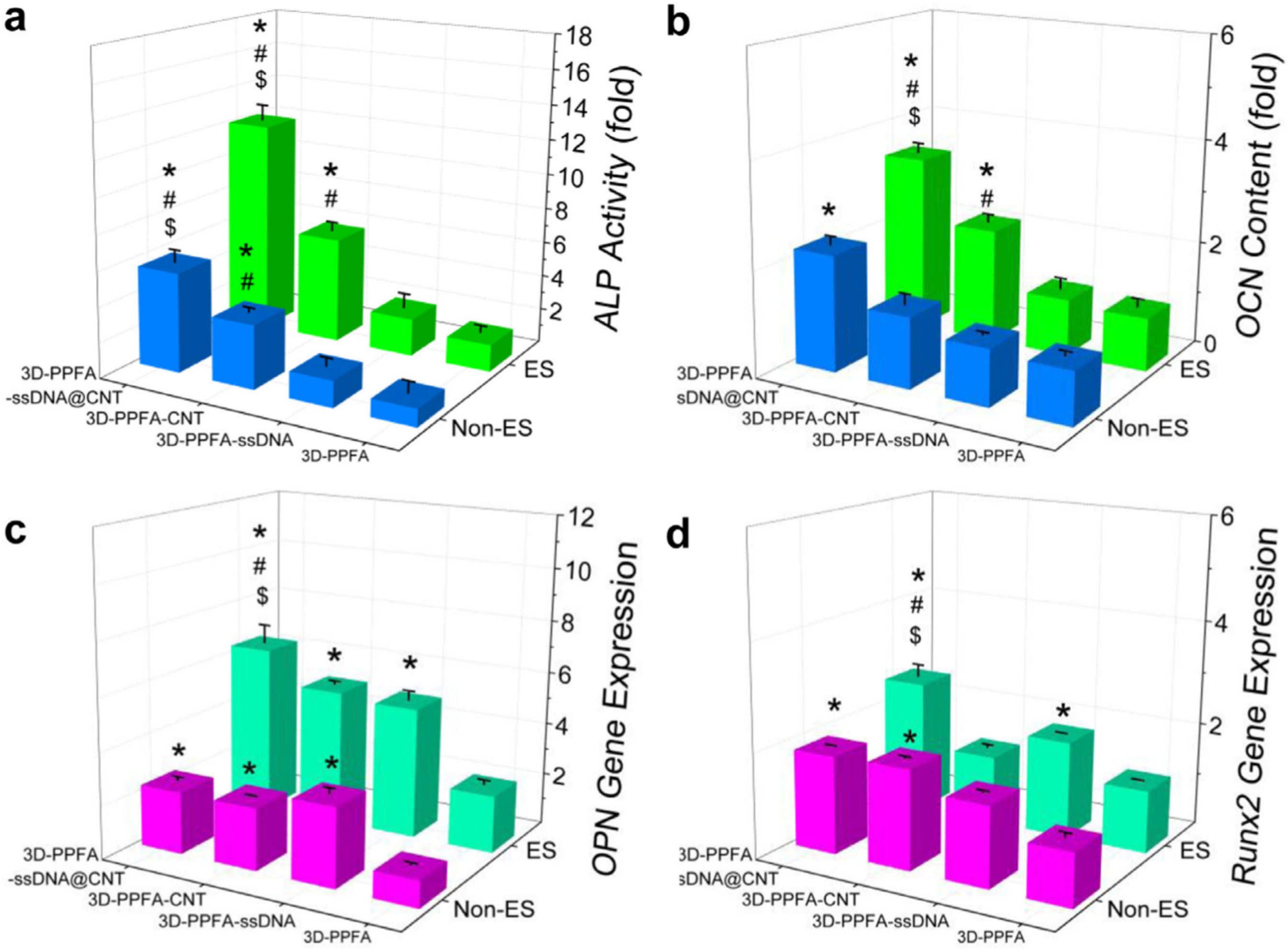

Fig. 6.

Osteogenic differentiation. a) Intracellular ALP activity in MC3T3 pre-osteoblasts on 3D-printed scaffolds under ES or non-ES conditions for 14 days. b) OCN content from pre-osteoblasts cultured on 3D-printed scaffolds under ES or non-ES condition for 21 days. RT-qPCR analysis of c) OPN and d) RUNX2 gene expression levels before and after electrical stimulation on each treatment for 14 days. The values within each test were normalized to the 3D-PPFA non-ES group (set as 1). *: $p < 0.05$ compared to 3D-PPFA group with same non-ES or ES treatment; #: $p < 0.05$ compared to 3D-PPFA-ssDNA group with same non-ES or ES treatment; $: $p < 0.05$ compared to 3D-PPFA-CNT group with same non-ES or ES treatment. (For interpretation of the references to color in this figure legend, the reader is referred to the web version of this article.)